ADVANCED MATERIALS
www.advmat.de

"Red Carbon": A Rediscovered Covalent Crystalline Semiconductor

Mateusz Odziomek, Paolo Giusto, Janina Kossmann, Nadezda V. Tarakina, Julian Heske, Salvador M. Rivadeneira, Waldemar Keil, Claudia Schmidt, Stefano Mazzanti, Oleksandr Savateev, Lorena Perdigón-Toro, Dieter Neher, Thomas D. Kühne, Markus Antonietti, and Nieves López-Salas**

Carbon suboxide (C_3O_2) is a unique molecule able to polymerize spontaneously into highly conjugated light-absorbing structures at temperatures as low as 0 °C. Despite obvious advantages, little is known about the nature and the functional properties of this carbonaceous material. In this work, the aim is to bring "red carbon," a forgotten polymeric semiconductor, back to the community's attention. A solution polymerization process is adapted to simplify the synthesis and control the structure. This allows one to obtain this crystalline covalent material at low temperatures. Both spectroscopic and elemental analyses support the chemical structure represented as conjugated ladder polypyrone ribbons. Density functional theory calculations suggest a crystalline structure of AB stacks of polypyrone ribbons and identify the material as a direct bandgap semiconductor with a medium bandgap that is further confirmed by optical analysis. The material shows promising photocatalytic performance using blue light. Moreover, the simple condensation–aromatization route described here allows the straightforward fabrication of conjugated ladder polymers and can be inspiring for the synthesis of carbonaceous materials at low temperatures in general.

1. Introduction

Organic and polymeric semiconductors with in-plane π-conjugated systems have gained enormous attention in the last two decades, especially in the field of solar cells and solar-to-chemical energy conversion.[1] The latter was particularly accelerated by the demonstration of photocatalytic water splitting over carbon nitride.[2] Since then, many different polymeric semiconductors have been developed, including graphene analogs, covalent organic frameworks, or conjugated ladder polymers.[3,4] The control over the spatial extension of π-conjugation, the structuration, the type and content of heteroatoms, and/or defects allows tailoring their final properties. The synthesis of extended π-conjugated systems, especially model carbon materials, usually requires high temperatures, leading to the lack of rational chemical control over the structure. Therefore, it is necessary to look for new routes toward conjugated carbonaceous materials that avoid harsh conditions and thus allow for better control of the resulting structure.

The synthesis under mild conditions requires new concepts such as new monomers or smart condensation–aromatization routes. This could provide necessary tools for a better design of covalent semiconductors. A good example is the synthesis of graphene nanoribbons by Müllen and Feng.[5–7] They used dehalogenation–cyclodehydrogenation or Diels–Alder

M. Odziomek, P. Giusto, J. Kossmann, N. V. Tarakina, J. Heske, S. Mazzanti, O. Savateev, M. Antonietti, N. López-Salas
Colloids Chemistry Department
Max Planck Institute of Colloids and Interfaces
Am Mühlenberg 1, 14476 Potsdam, Germany
E-mail: mateusz.odziomek@mpikg.mpg.de; nieves.lopezsalas@mpikg.mpg.de

The ORCID identification number(s) for the author(s) of this article can be found under https://doi.org/10.1002/adma.202206405.

DOI: 10.1002/adma.202206405

J. Heske, S. M. Rivadeneira, T. D. Kühne
Dynamics of Condensed Matter and Center for Sustainable Systems Design
Chair of Theoretical Chemistry
Paderborn University
Warburger Str. 100, D-33098 Paderborn, Germany

W. Keil, C. Schmidt
Department of Chemistry
Physical Chemistry
Paderborn University
Warburger Str. 100, 33098 Paderborn, Germany

L. Perdigón-Toro, D. Neher
Soft Matter Physics and Optoelectronics
University of Potsdam
Karl-Liebknecht-Straße 24–25, 14476 Potsdam, Germany

reaction–cyclodehydrogenation cascades as condensation–aromatization routes. Although their methods give atom-resolved structures, they rely on graphoepitaxy, resulting in very low product yields.

The novel routes toward conjugated ladder or in-plane systems do not necessarily need to be "new." The story of carbon nitride which was discovered and re-discovered at least three times in the past 100 years teaches us to look back into the "old" literature.[8] Carbon suboxide, a member of the carbon oxide family, and its condensates are examples of widely forgotten materials that await re-discovery. Their story started in the 19th century when Brodie obtained C_3O_2 from CO in an induction tube and reported its spontaneous condensation to red solids named "red carbon" (herein, $p(C_3O_2)_x$).[9] The formation and properties of red carbon were the subject of few studies in the past century, giving the picture of a semiconducting material with potentially semimetallic properties.[10–15] Since then, the interest in $p(C_3O_2)_x$ has somewhat vanished, and its application potential has never been thoroughly studied.

C_3O_2 can be synthesized at temperatures as low as 140 °C, by dehydration of malonic acid (MA) over P_2O_5.[15] Subsequently, it polymerizes spontaneously already at room temperature to a dark solid, with rates difficult to control that depend on the temperature and the presence of impurities. Moreover, the polymerization time and the properties of the polymer reported in the early literature differ, indicating its high sensitivity to synthetic conditions. This, together with characterization techniques that were less advanced than today, might be one of the reasons for the loss of interest in the material. The currently accepted model describes the structure of $p(C_3O_2)_x$ as a conjugated ladder made of fused α-pyrone units forming polypyrone chains.[16] However, its functional properties were never explored.

Herein, we establish a simple solution process to synthesize $p(C_3O_2)_x$ and analyze its potential application in photocatalysis. Taking inspiration from nature for the synthesis of highly conjugated molecules at ambient conditions, we activated carboxylic groups of MA by converting them to mixed anhydrides with acetic anhydride (AAn). Such mixed anhydrides are very reactive toward nucleophilic substitution because acetate is an excellent leaving group.[17] Liquid phase dehydration with AAn replaced the solid-state reaction of MA and P_2O_5 producing for the first time crystalline $p(C_3O_2)_x$, indicating improved quality and reproducibility. A broad range of analytical techniques confirmed that the structure and properties of the synthesized material are in agreement with previously reported $p(C_3O_2)_x$, thus validating the new synthetic pathway. The theoretical and structural analyses showed that the synthesized material is a crystalline organic semiconductor with a medium and tunable bandgap. An advantage of its structure is a good processability, in contrast to other polymeric semiconductors as, for example, carbon nitrides.[18] The red carbon is soluble in solvents with medium polarity and thus can be coated onto different substrates. This makes the material potentially attractive for many applications, such as organic light-emitting diodes (OLEDs),[19] organic field-effect transistors,[20] solar cells,[21] or photocatalysts.[22] For the first time, we investigated the optical and photocatalytic properties of red carbon. The system was able to catalyze the conversion of benzyl alcohol to benzaldehyde and of thioanisole into the corresponding sulfoxide and sulfone in yields exceeding those of state-of-the-art covalent semiconductors.

2. Results

2.1. Acetic Anhydride Approach

Several synthetic routes lead to C_3O_2, however, the dehydration of MA is the most convenient and affordable one. The reaction of a solid mixture of P_2O_5 and MA is an abrupt and self-accelerating process producing gaseous C_3O_2, which has to be collected in a cooling trap. Even after purification of the monomer by repeated distillation, the rate of polymerization and properties of $p(C_3O_2)_x$ differ between reports.[14] In contrast, solution polymerization allows a better management of the released heat and the reaction rate. Therefore, we developed an alternative liquid-based process to synthesize $p(C_3O_2)_x$ with much higher throughput and greater structural control. AAn served as both a dehydrating agent and a liquid medium for the reaction. In addition, the side product acetic acid is reported to have a catalytic effect on the reaction.[14]

MA mixed in different proportions with AAn was heated to 110 or 140 °C for 5 h. Sequentially, the solution turned yellow, orange, red, and dark ruby, manifesting the condensation process (**Figure 1**a). At the end of the reaction, the solution was viscous, almost black, but when spread over a glass slide, it reflected a deep red or red-brown coloration, depending on the conditions. Subsequently, the compound was precipitated from diethyl ether, filtrated, and washed with diethyl ether. Figure 1b shows the hypothetical reaction mechanism starting from the formation of the mixed malonic–acetic anhydride (and concomitant release of acetic acid). Inter- or intra-molecular subtraction of an acidic alpha hydrogen atom from MA at elevated temperature forms a ketene group on one side, facilitated by the good leaving acetate group. Malonic acid anhydride (oxetane-2,4-dione) has never been detected in the products of MA dehydration.[23] This suggests that the second dehydration is energetically favorable and thus probably occurs spontaneously after the first one, producing C_3O_2. ^{1}H NMR and ^{13}C NMR studies performed on aliquots of the reaction mixture at different stages support the proposed mechanism. The NMR signals of MA gradually disappeared concomitantly with appearing peaks from acetic acid and mixed anhydride (Figures S1 and S2, Supporting Information), the latter only being an intermediate and also vanishing soon.

2.2. Structural and Chemical Analysis

Table 1 summarizes the synthetic conditions, the reaction yields, and selected properties of the fabricated samples. The reaction yield is proportional to the AAn:MA ratio and it is slightly higher for reactions at 140 °C. This is not surprising since one molecule of MA theoretically needs two molecules of AAn to withdraw two molecules of water. The relatively low yields are ascribed mostly to the thermal decomposition of malonic acid to acetic acid and CO_2. Moreover, the generated C_3O_2 is also

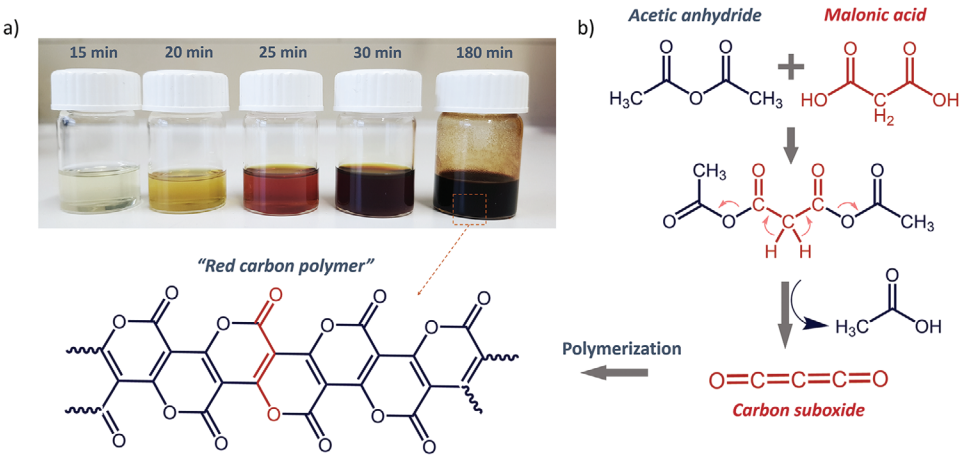

Figure 1. Acetic anhydride synthetic route toward $p(C_3O_2)_x$. a) Digital picture of the reaction mixture at different stages. b) Proposed reaction mechanism via the activation of malonic acid by the formation of mixed anhydride.

a gaseous product at this temperature, so it can easily escape from the reaction mixture. Furthermore, side products can be produced during the dehydration of malonic acid. According to gas chromatography coupled with mass spectroscopy, dehydroacetic acid was the main byproduct detected (Figure S3, Supporting Information). On top of that, smaller molecular weight $p(C_3O_2)_x$ oligomers were also extracted during washing leading to further yield losses.

The elemental analysis revealed that the molar ratio of C:O of all the products fluctuates around 1.5, the theoretical value expected for $p(C_3O_2)_x$. The analysis also shows the presence of about 2 wt% of H (Table S1, Supporting Information), which might originate from impurities, end-groups or simply from adsorbed water. The structural and morphological analyses confirmed the strong similarities between red carbons synthesized under different conditions. For simplicity, we discuss the typical results for the case of sample 1:2_140. The data for all other samples are given in the Supporting Information, while significant variations of properties between the samples are discussed in the text.

To elucidate the molecular mass of $p(C_3O_2)_x$, we performed gel permeation chromatography with the samples dissolved in *N*-methylpyrrolidone (NMP) (Figure S4, Supporting Information, and Table 1). The results show a clear trend in average molecular weight (M_w) which grows from 825 to 1867 g mol^{-1} by rising the AAn:Ma ratio and the temperature. All samples are rather in the oligomer than in the polymer range. The number average molecular weight (M_n) is between 637 and 951 g mol^{-1} resulting in only moderate polydispersity of the samples as calculated by the M_w/M_n ratio. The average molecule contains between 8 and 19 pyrone units. These values are higher than previously reported[13,14] except for one SAXS study in which 40 monomer units were found.[24] However, the molecular weight determined by gel permeation chromatography (GPC) must be taken with a grain of salt due to the lack of an appropriate standard. The dynamics of rigid conjugated ladder polymers differ significantly from non-rigid ones like polystyrene which is often used as standard in GPC analysis of molecular weight.[4]

The X-ray diffraction (XRD) pattern in **Figure 2**a reveals four intense peaks at 2θ values of 18.3°, 19.0°, 24.6°, and 32.7°, corresponding to lattice distances of 0.48, 0.47, 0.36, and 0.27 nm, respectively, and a low-angle reflection at about 5 (1.8 nm). The distance of 0.36 nm most likely relates to the interplanar spacing between polypyrone chains, while the others are associated with in-plane distances. The low angle peak is characteristic of ordered nanostructures and indicates the formation of a sort of mesophase with a distance related to the lateral

Table 1. Synthetic conditions and selected properties of the prepared samples. M_w, PDI, and M_p denote mass average molar mass, polydispersity index, and peak molar mass.

	Synthesis			Properties		GPC – parameters		
Name	AAn : Ma [mol mol^{-1}]	Temp [°C]	Yield[a)] [%]	C:O [mol mol^{-1}]	Band gap [eV]	M_w [g mol^{-1}]	PDI	M_p [g mol^{-1}]
1:1_110	1:1	110	3.0	1.40	1.93	825	1.30	637
1:1_140	1:1	140	4.7	1.50	1.82	1027	1.61	640
1:2_110	2:1	110	8.8	1.41	1.84	988	1.52	650
1:2_140	2:1	140	9.6	1.57	1.79	1189	1.75	679
1:5_110	5:1	110	15.9	1.53	1.82	1060	1.52	698
1:5_140	5:1	140	20.4	1.64	1.74	1867	1.47	951

[a)]Yield calculated with respect to the theoretical amount of carbon suboxide from malonic acid.

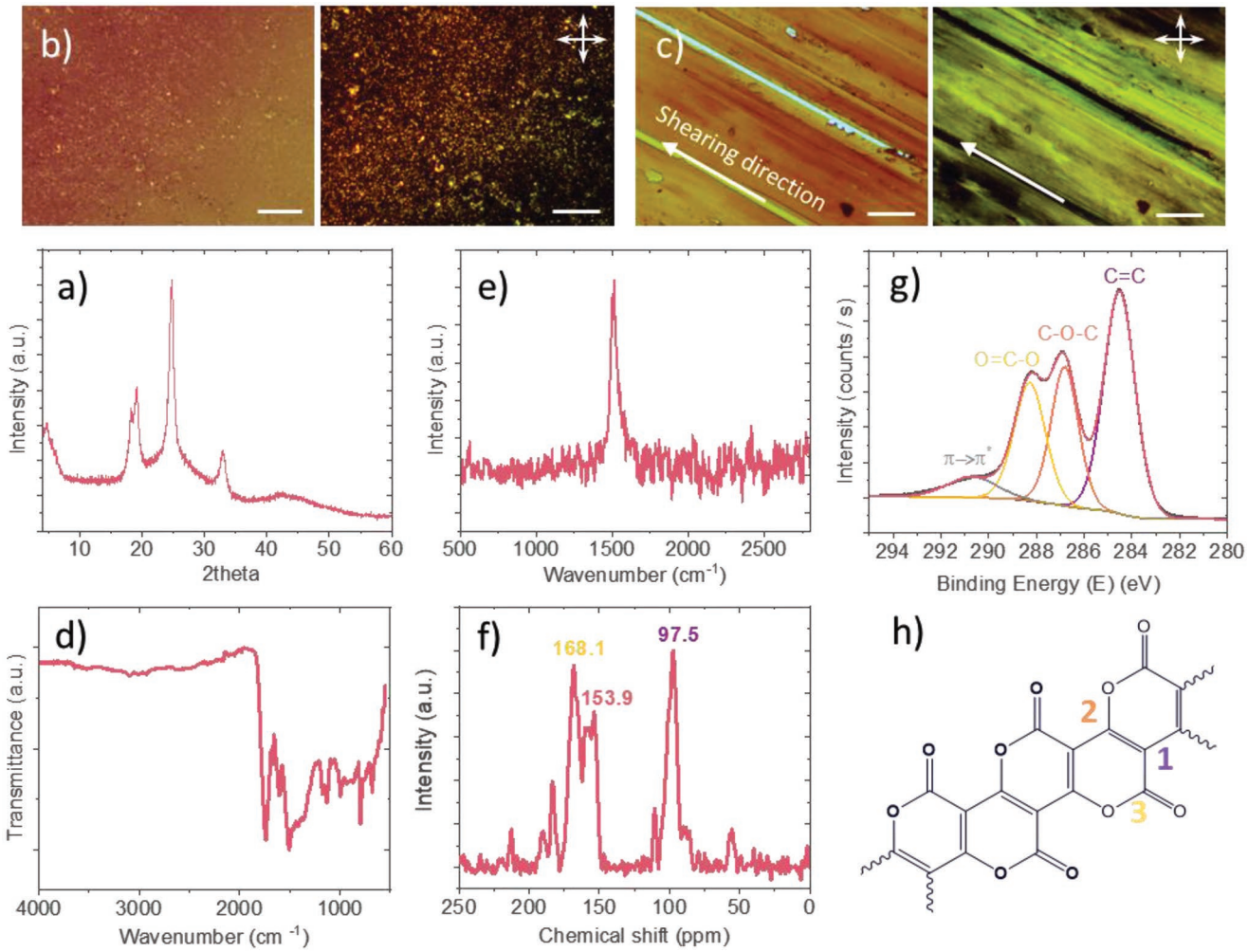

Figure 2. Structural analysis of $p(C_3O_2)_x$ sample 1:2_140. a) XRD pattern revealing the crystallinity of $p(C_3O_2)_x$. b) Optical microscope pictures of drop-casted sample from DMF solution under normal (left) and cross-polarized light (right), scale bar = 30 µm. c) Optical microscope pictures of oriented mesocrystals in a single direction under normal (left) and cross-polarized light (right). The powder was spread over a glass slide in the direction marked by the arrow. Scale bar = 30 µm. d) FTIR spectrum. e) Raman spectrum characteristic for polyacetylene-like structure. f) Direct polarization ^{13}C MAS NMR spectrum confirming the structure of the material based on polypyrone units; the colors of the chemical shifts correspond to the color of carbon atoms assigned in the sketch of a fragment of a polypyrone ribbon (h); g) C 1s XPS with deconvoluted peaks; the color of deconvoluted peaks corresponds to the color of carbon atoms assigned in the sketch (h).

or longitudinal size of $p(C_3O_2)_x$ in the crystalline domain.[25] Especially the fact that the position of the peak slightly shifts between samples might indicate the correlation of peak position to the size of the ribbons (Figure S5, Supporting Information). Indeed, the rigid molecular structure of the oligomer directs the formation of calamitic liquid-crystal like phases.[26] The presence of a peak in the small angle region (<10° 2θ) indicates the formation of smectic-like phases with clear interlayer spacing.[27] The distance of the peak corresponding to about 1.8 nm matches well the size of the oligomers determined by GPC. An oligomer of ten fused pyrone units is about 1.9 nm long. The relatively large width of the peaks is indicative of crystallites in the nanometer range, the presence of strong distortion in the crystals induced by different sizes of the polypyrone ribbons, or the presence of defects in the structure.[28] This might be a reason why $p(C_3O_2)_x$ was previously reported as an amorphous material.[12,16] Nearly all reported syntheses were based on the reaction of pure C_3O_2 monomer, which also might suppress crystallization for mobility reasons.

The highly crystalline character of the sample was also clearly observed with an optical microscope where plenty of bright spots appear under polarized light (Figure 2b). Furthermore, the liquid-crystal like behavior is observed when the solid sample is spread over the substrate using friction forces. The powder sample was spread with a spatula over the glass substrate. This causes the formation of a film with uniform crystal orientation in the direction of the friction forces (Figure 2c). Under polarized light, the film is uniformly bright (the Figure 2c [right] and Figure S6a,c, Supporting Information) or completely dark (Figure S6b,d, Supporting Information) depending on the rotation angle with respect to the polarizers, proving the uniform nature of the sample and the orientation of the mesostructure.

Like XRD, Fourier-transform infrared spectroscopy (FTIR) (Figure 2d and Figure S7, Supporting Information) does not

show significant differences between the samples, pointing at a uniform chemical nature. The broad band composed of overlapping peaks between 1800 to 500 cm^{-1} confirms the strongly conjugated character of the compounds. The intense peak at 1740 cm^{-1} is ascribed to C=O observed in unsaturated lactones (such as coumarin), an assignment further confirmed by the two bands at 1170 and 1130 cm^{-1} that are characteristic of C—O bonds. This supports the presence of pyrone units in the structure of $p(C_3O_2)_x$. The peaks between 1600 and 1350 cm^{-1} originate from different stretching vibration modes of C=C bonds. A relatively strong band at 800 cm^{-1} appears in all FTIR spectra of reported red carbon but is rarely discussed. In the literature, such band was reported for collective vibration of adjacent ether configurations at the edge of graphenic structures.[29] In $p(C_3O_2)_x$, similar adjacent O groups at the edge exist and most likely are responsible for this band. It is worth mentioning that the FTIR spectra of $p(C_3O_2)_x$ in the literature significantly differ, suggesting a strong influence of the preparation conditions on the structure.[12,13,15,16] The FTIR spectra of the samples contain either no or just weak bands around 3000 cm^{-1}, typically attributed to —OH and $—CH_x$ groups, whereas, in the literature, the samples exposed to humid air featured strong bands from —OH groups.[15] Raman spectra turned out to be very challenging to record since $p(C_3O_2)_x$ tends to decompose even using low laser power, giving G and D bands typical for carbon structures (Figure S8, Supporting Information).[30] Very low laser power and long acquisitions finally resulted in a true spectrum of $p(C_3O_2)_x$ with a single peak at 1513 cm^{-1} which is assigned to alternating C=C and C—C stretching modes (Figure 2e). The single peak is relatively sharp and well resolved indicating homogeneity of the structure. The spectrum corresponds well to polyacetylene which can be seen as part of the $p(C_3O_2)_x$ structure.[31,32] In polyacetylenes, Raman spectra show an additional peak coming from C—H bonds (around 1100 cm^{-1}). However, in $p(C_3O_2)_x$ the C—H groups are replaced by —O—C(O)— bridging two neighboring C=C. The resonances from C=O or C—O are perhaps too weak to be seen as such low laser power is inactive for Raman.

The ^{13}C magic angle spinning (MAS) nuclear magnetic resonance (NMR) spectrum (Figure 2f) recorded by direct polarization confirms a highly conjugated nature of $p(C_3O_2)_x$ by the presence of peaks almost exclusively in the region above 90 ppm, which are assigned to sp^2 carbons. The cross-polarization ^{13}C MAS NMR measurement, even after sampling of 8192 scans, did not yield a reasonable signal confirming that hydrogen atoms are essentially absent in the structure. We note that direct polarization intensity ratios are not quantitative, due to long spin-lattice relaxation times (T_1), especially for the rigid sp^2 carbon sites. The three strongest peaks correspond well to the three different carbons in the structure of $p(C_3O_2)_x$ (Figure 2h).[16] The peaks at 168.1 and 153.9 ppm arise from the carbonyl carbon of the lactone group (O—C=O) and the sp^2 carbon atom connected to one oxygen only, respectively. The peak at 97.5 ppm comes from sp^2 carbon sites not connected to a heteroatom and represent very electron-rich aromatic positions. The otherwise typical aromatic sp^2 peak is expected at 128 ppm, and only some special conjugated carbons in dye structures are as electron rich as these specific carbons. The small signals above 180 ppm might originate from carboxylic groups located at the end of the polypyrone ribbons, impurities, or defective sites in the chain. A tiny peak above 200 ppm indicates the presence of ketone groups most likely associated with side reactions, such as ketene dimerization and the formation of compounds as dehydroacetic acid. Another peak of low intensity, located at 110 ppm, in the region typical for aromatic structures might indicate the onset of possible thermal degradation of the red carbon.

X-ray photoelectron spectroscopy (XPS) analysis further confirmed the presence of three different carbon sites. Figure 2g shows the deconvoluted C1s XPS spectrum of the sample 1:2_140. The deconvolution comprises three major peaks centered at 288.9, 286.6, and 284.5 eV with similar broadening, corresponding to carbon atoms attached to two, one and no oxygen atoms, respectively (as indicated in Figure 2h). The presence of a strong π–π satellite peak centered at 290.9 eV corroborates the highly conjugated nature of the material. All other compounds have similar spectra, however, the relative peak intensity differs slightly (Figure S9, Supporting Information).

Despite the simplified solution synthesis, the structural analysis and appearance of the sample are in good agreement with the previous reports. With the in situ generated monomer, the "in solution" reaction benefits from the homogeneous initiation/nucleation and growth reaching larger molecular weights. The relatively high crystallinity of the sample reflects the uniformity of polypyrone ribbons. Their rigidity and planar shape facilitate the formation of the crystalline phase during aggregation from solution. Beyond that, we cannot exclude the presence of defects like open lactone rings, some carbon-rich regions depleted from oxygen by elimination of CO_2, or the presence of impurities that are difficult to remove, such as ketene dimers and their follow-up products. The thermal stability and thermal decomposition mechanism quantified by thermogravimetric analysis are the same as in previous reports (Figure S10, Supporting Information).[13] This decomposition mechanism forbids increasing the synthetic temperature to increase the yield of the reaction but, at the same time indicates that, at higher temperatures, the cross-linking of the C_3O_2 oligomers through thermal decarboxylation may lead to the synthesis of carbon-based materials. The results give the picture of one-dimensional band-like oligomers, which form a sort of molecular crystal rather than a semi-crystalline structure. It is also clear that the explored synthetic conditions had rather minor effects on the properties of red carbon. The increase of the AAn:Ma ratio considerably enhances the yield of the process but only slightly increases the sample molecular weight. This is probably because of the reduced solubility of the oligomers in the reaction medium that, once achieving a certain size, precipitate hampering further growth. Therefore, a higher amount of AAn has a negligible effect on the properties.

The similarities of all samples are further confirmed by scanning electron microscopy (SEM) (Figure S11, Supporting Information). Their morphology is a mixture of nanosheet- and nanoribbon-like species formed upon precipitation from diethyl ether. The sample synthesized at 110 °C forms more sheets-like species, while the one synthesized at 140 °C produces more nanoribbon-like species. This morphology change is likely due to the different sizes and distribution of the polypyrone chains.

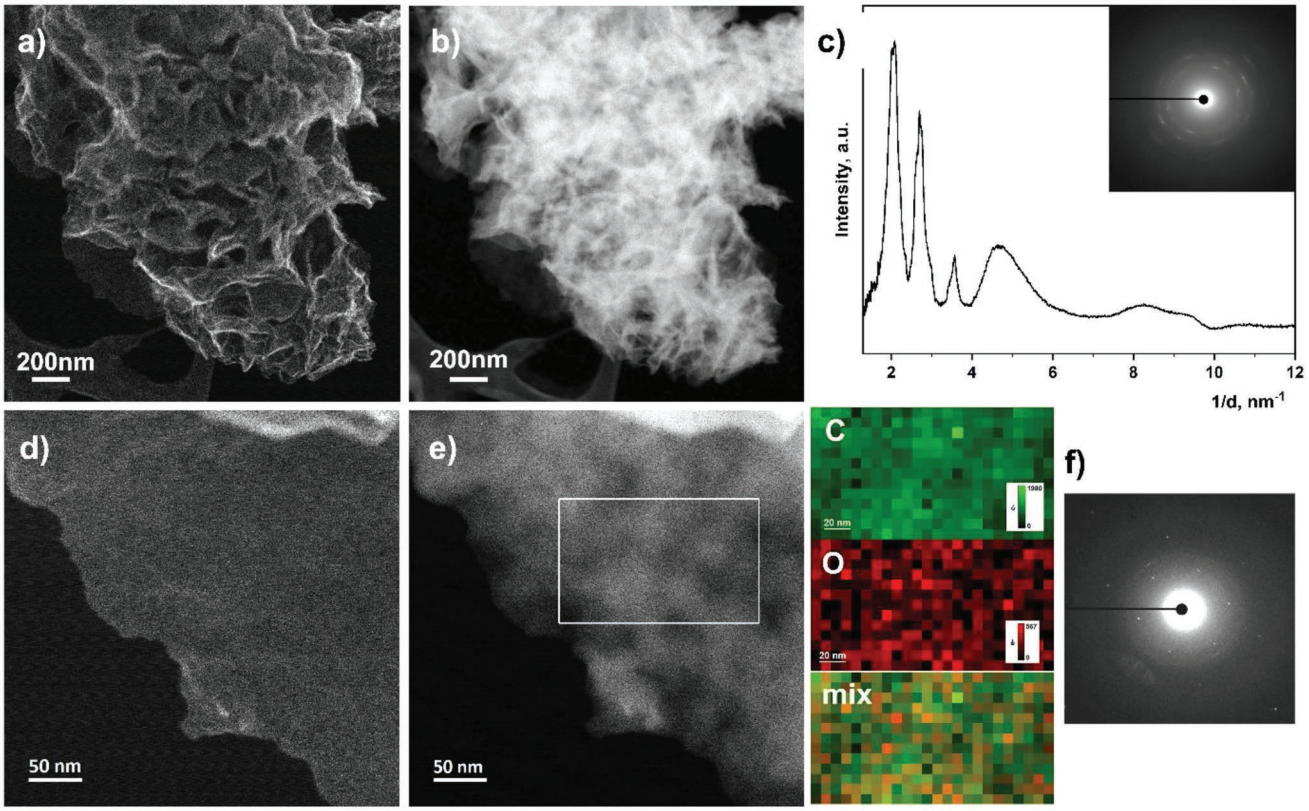

Figure 3. Scanning transmission electron microscopy. a,d) Secondary electrons STEM images. b) Annular dark-field STEM images. c) Azimuthal averaging intensity profile obtained from the SAED pattern of non-flat particles shown in the inset. e) Annular dark-field STEM image of the area shown in (d) and corresponding EELS maps of carbon, oxygen, and overlap of both signals. F) Single crystalline SAED pattern obtained from flat flakes.

Energy dispersive X-ray analysis (EDX) further confirmed the sample composition. Each sample contained around 60 at% of carbon and 40 at% of oxygen (Figure S11, Supporting Information). Although the samples seem to possess textural porosity at first glance, N_2 sorption analysis revealed only a small volume fraction of nanopores, with the Brunauer–Emmett–Teller (BET) surface area not exceeding 85 m^2 g^{-1} for sample 1:2_140 (Figure S12, Supporting Information).

Scanning transmission electron microscopy was performed on sample 1:2_140 (**Figure 3**). Two types of morphologically different particles were found in the sample. The first type has the appearance of crumpled paper (Figure 3a,b), which is typical for polymeric materials and in most cases shows weak rings on the selected area electron diffraction (SAED) patterns with the same *d*-distances as found on the XRD patterns (Figure 3c). The second type corresponds to flatter separate particles or flat areas of the first type of particles (Figure 3d,e) and gives single crystalline SAED patterns with pseudo hexagonal 2D symmetry and *d*-distances corresponding to the XRD peaks at about 19.0 and 32.7 (2θ) (Figure 3f). Electron energy-loss spectra (EELS) collected from flat areas of the flakes confirmed the presence of both carbon and oxygen; both signals have a relatively uniform distribution at the nanoscale (Figure 3e). The C K-edge has a very low intensity π^*-peak (shoulder) and a σ^*-peak displaying no specific fine structure features (Figure S13, Supporting Information).

2.3. Theoretical Studies

To investigate the atomistic structure and to better understand the molecular properties of $p(C_3O_2)_x$, a second-generation Car–Parrinello-based dynamical simulated annealing to search for low-lying minima of the energy landscape was performed using semi-local density functional theory (DFT) using the CP2K code.[33,34] The lowest energy structure found is a planar 2D structure of adjacent infinite C_3O_2 monomers (see **Figure 4**a,c). This molecular structure agrees with the schematic representation in Figure 1. The outer oxygens are decisive for the orientations of the ribbons with respect to each other. As can be seen in the horizontal electron distribution of a C_3O_2 layer in Figure 4b as well as in the DDEC6 charge analysis (Figure 4f),[35] they carry the highest electron density (net charge = –0.39) and therefore repel each other. This leads to a displacement of half a pyrone unit with respect to each other in plane, resulting in a distance of 4.0 Å between the oxygen atoms of adjacent $p(C_3O_2)_x$ chains. The same argumentation also applies to the stacking of $p(C_3O_2)_x$. The repulsion of electrons localized at the oxygen atoms (Figure 4d) leads to the fact that an AA stacked $p(C_3O_2)_x$ is energetically significantly higher than the eventual structure, which is AB stacked as seen in Figure 4c. The vertical distance between the different stacked C_3O_2 planes is 3.7 Å, which corresponds to the peak at around 24° of the calculated XRD of the AB stacked structure (Figure 4e), as well as the high

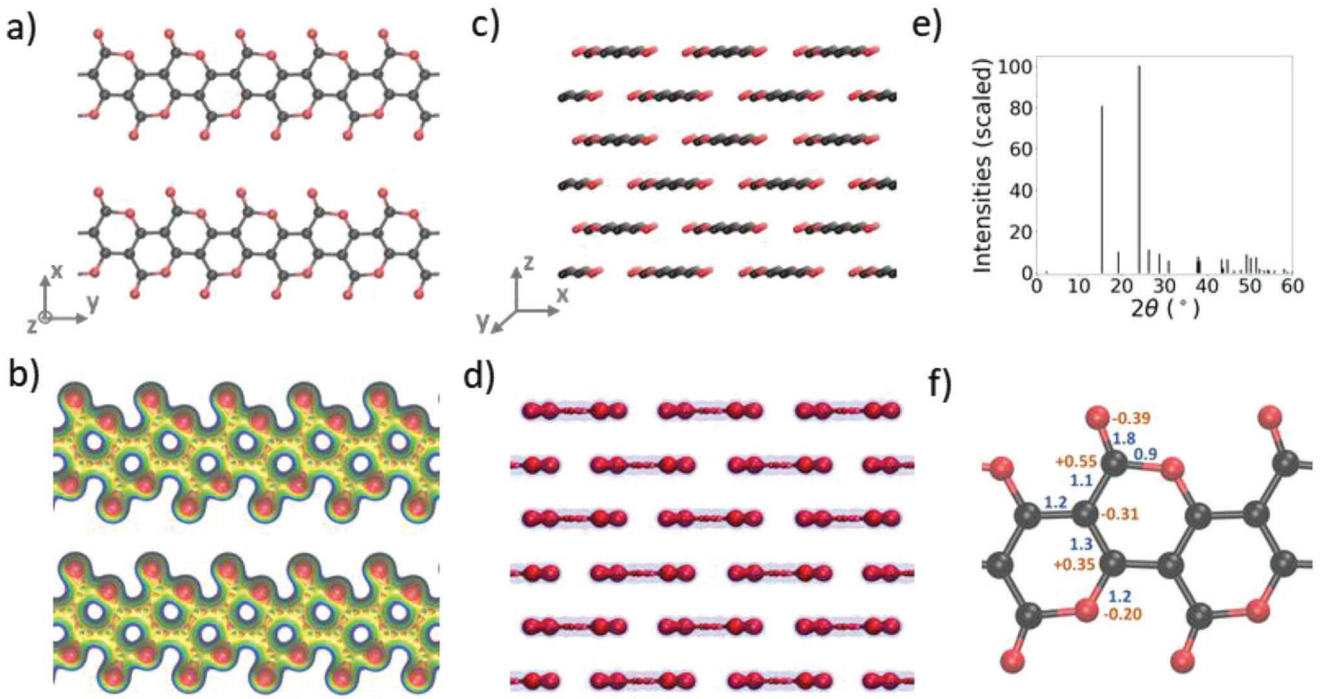

Figure 4. a) Top view of a single layer of $p(C_3O_2)_x$, b) in-plane electron density distribution (red: high, blue: low), c) lateral view of the periodic AB stacked $p(C_3O_2)_x$ model, d) lateral view of the electron distribution over $p(C_3O_2)_x$ ribbons, e) the corresponding calculated XRD, and f) the calculated DDEC6 net atomic charges (orange) and bond orders (blue).

intensity peak in the measured XRD pattern (Figure 2a). Furthermore, the electron density distribution shows that the rest of the electrons not accumulated at the electron-rich oxygens are delocalized over the entire conjugated system, thereby stabilizing the system. At the present semi-local DFT level of theory, which is known to underestimate the true fundamental gap, the obtained model of $p(C_3O_2)_x$ has a direct band gap of 1.52 eV. The modeled structure does not consider the length and polydispersity of the oligomeric units, which is the main source of discrepancies with experimental XRD data. For instance, the low angle XRD peak at 5° (2θ) is the result of mesostructuration caused by the finite size of oligomers. Therefore, it is not observed in the XRD from the model structure. In addition to the limitations in the size of the oligomers, the end groups can play an important role in the mutual interaction between ribbons.

2.4. Optical Properties and Processability

To elucidate the electronic properties of the material, UV–vis absorption and photoluminescence (PL) spectroscopy were performed. The $p(C_3O_2)_x$ powder absorbs light in a broad range extending far into the infrared region (beyond 1000 nm) and reaching a plateau at about 400 nm (**Figure 5**a). The shape of the absorption curve is similar for each sample regardless of the synthetic conditions (Figure S14, Supporting Information). Based on the theoretical studies, we assumed for the calculations that the material is a direct band-gap semiconductor. Indeed, the absorption spectra can be analyzed in terms of Tauc plots (Figure S15, Supporting Information), which yield bandgaps ranging between 1.76 and 1.93 eV (Table 1). The results are in good agreement with the theoretical studies, and the difference in the absolute numbers might originate from the different sizes of the oligomers or the distorted π–π interactions in the synthesized material. The optical band gap is notably smaller than most applied organic and polymeric semiconductors, allowing absorbing light from a much broader spectrum.[36] Higher temperatures and higher AAn:MA ratios lower the optical band gap due to either a more extended conjugation (higher molecular weight of the polypyrone ribbons) or an enhanced stacking of larger molecular units into a crystalline structure. However, all spectra show a broad tail extending down to 1.5 eV or even below. This tail is most likely related to the heterogeneity of the samples with regard to conjugation length and intermolecular order.

The oligomeric nature of the solid sample and the absence of H-bridges allow dissolving $p(C_3O_2)_x$ in medium polar organic solvents like NMP and DMF, and partially in THF. $p(C_3O_2)_x$ is only weakly soluble in ethyl acetate and water. The UV–vis absorption spectrum of the diluted solution in NMP shows a narrow peak centered at 415 nm and no light absorption above 550 nm. This shows that the largely red-shifted absorption of the powder sample is due to intermolecular interactions in the π–π stacked crystalline domains.

The absorption coefficient of the solubilized red carbon is equal to 59.1 L g^{-1} cm^{-1} at 415 nm, as calculated using the Lambert–Beer law. Considering that the average molar mass of $p(C_3O_2)_x$ ranges between 700 and 1200 g mol^{-1}, this corresponds to molar absorption coefficient values between

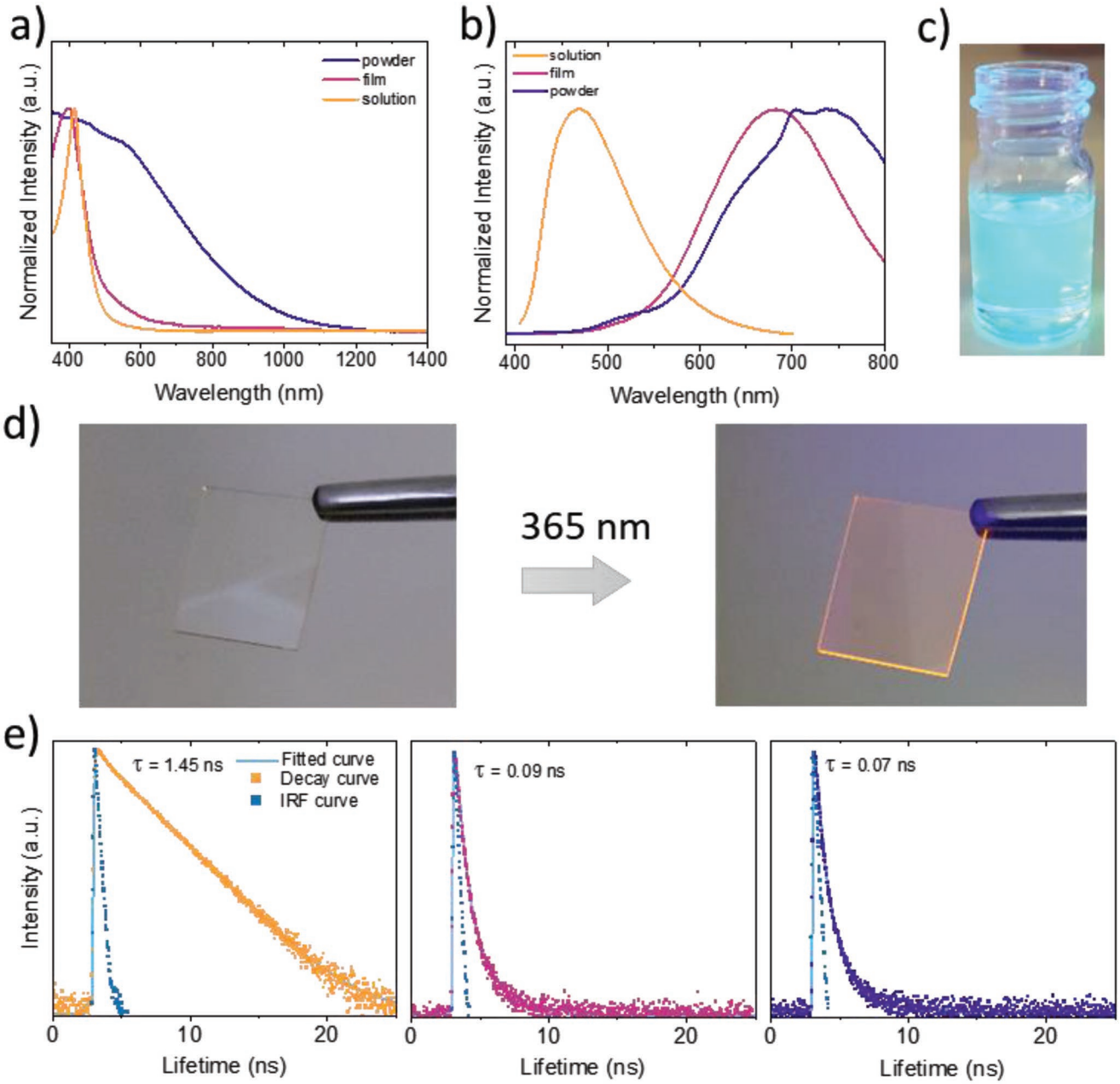

Figure 5. Optical properties of $p(C_3O_2)_x$ 1:2_140. a) UV–vis absorption of $p(C_3O_2)_x$ in the form of powder, film and a 0.0002 wt% solution in NMP. b) Steady-state photoluminescence spectra upon excitation at 370 nm. c) Picture of the bright photoluminescent emission of 0.0002 wt% $p(C_3O_2)_x$ solution in NMP irradiated with a UV lamp (365 nm). d) Spin-coated film on a glass slide under ambient light (left) and exposed to UV lamp (right). e) corresponding photoluminescence decay curves for solution (orange), film (violet), and powder (purple) excited with 375 nm laser and light collected at 480 nm (solution), 670 nm (film), and 680 nm (powder).

4.1×10^4 and 7.1×10^4 M^{-1} cm^{-1}, which are higher than the benchmark organic dyes used in photovoltaics (e.g., polythiophenes).[37] Such high absorption supports the strong rigidity of the conjugated ladder polymer. Generally, coiled polymers show lower oscillatory strength and thus lower absorption.[38] The light absorption strongly depends on the solvent properties, as observed in many other organic systems. The oligomers of red carbon show a hypsochromic shift with increasing solvent polarity (Figure S16, Supporting Information). Regardless of the synthetic conditions, all samples have a maximum absorption at 415 nm in NMP but more conjugated structures show a significant broadening of the absorption (Figure S17, Supporting Information). This can be explained on the basis of their molecular weight distributions, where the presence of larger chains is most likely responsible for absorption broadening.

The solubilized $p(C_3O_2)_x$ can be processed into a film. Using a simple spin-coating technique, homogeneous and transparent films could be fabricated (Figure 5d). The optical absorption is

very similar to that in solution, showing that intermolecular effects in the amorphous film have a minor effect on absorption. This suggests a rather random orientation of the majority of the $p(C_3O_2)_x$ ribbons in contrast with the solid-state sample, wherein strongly red-shifted light absorption indicates strong intramolecular electronic coupling between the polypyrone ribbons and their coplanar geometry.

When excited with UV light, both the solution and the film show bright PL, however, with very different color (Figure 5b–d). The PL spectrum of the powder sample exhibits a broad maximum with two distinct peaks at ≈700 nm (1.77 eV) and 745 nm (1.66 eV), consistent with an optical bandgap of 1.79 eV as determined from the absorption spectra. However, there is additional higher energy emission which, in accordance with the interpretation of the absorption spectra, is assigned to emission from less crystalline regions. Note that the PL spectra was recorded using an excitation wavelength of 370 nm, which excites merely all chains present in the sample. In contrast to the PL response of the powder, one of the dissolved oligomers peaks at ≈475 nm, with a fairly small Stokes shift of 60 nm with respect to the absorption. This points to a rather rigid structure of the dissolved oligomers.[39] Surprisingly, the $p(C_3O_2)_x$ exhibits strong PL emission from NMP while in DMF the emission was strongly suppressed as can be seen by irradiation of the samples with UV light (Figure S18, Supporting Information). We do not have a clear explanation for such behavior but it has been previously reported that conjugated polymers in some solvents might form intermolecular CT states suppressing the PL quantum yield.[40] Similarly to absorption, photoluminescent emission also exhibit hypsochromic shift with increasing solvent polarity (Figure S19, Supporting Information). Interestingly, the PL of the film sample is similar to that of the powder sample, though its absorption differs only slightly from that of the dissolved chains. As such, this sample shows a large Stokes-shift which in films of amorphous oligomers and polymers has been interpreted as an efficient energy transfer from shorter (more blue absorbing) polymer segments to more conjugated chains, from which the majority of emission origins.[41] In the present samples, different molecular weight may be of less importance. Rather than that, the thin film absorption is dominated mostly by disordered regions which transfer their energy to few but strongly red-emitting crystalline areas.

The intense emission of solubilized red carbon in NMP was quantified by measuring relative quantum yield using Coumarin 153 as a fluorescent standard. The sample exhibited a relatively high quantum yield of 44%. Furthermore, the external quantum efficiency of the film was determined upon excitation at 440 nm. It was equal to 1.4×10^{-3}, which is in the range of p-type polymers in the solid state such as those used for solar cells.[42] Emission from the crystalline solid powder is even weaker, not observable by the naked eye, and even more red-shifted than the film. There are many possible reasons for the reduced PL efficiency in the solid state. For example, excitations may diffuse to defects which act as quenching sites. However, the coplanar packing of the molecules in the crystalline domains may also cause the formation and stabilization of non-radiative intermolecular CT states, being a likely cause for the drastic reduction of the PL efficiency when going from solution to the crystalline powder samples order.[40]

The kinetics of PL of red carbon in different states was measured using time-correlated single-photon counting (TC-SPC) time-resolved PL (Figure 5e), which allowed to determine PL emission lifetimes. The emission wavelength has been chosen to be at or close to the respective maximum of steady state emission. In liquid phase, the sample exhibit almost monoexponential decay with a lifetime $\tau = 1.45$ ns. Such behavior indicates a relatively low fluorescence quenching being in accordance with the high quantum yield. In the solid state and in the form of spin-coated films, the decay is more complex and cannot be fitted by monoexponential functions. Therefore, their lifetimes were calculated as average amplitude lifetimes using a triple stretched exponential fitting $\left(\bar{\tau} = \frac{\sum a_i \tau_i}{\sum a_i}\right)$,[37] commonly applied to photocatalysts as carbon nitrides. The calculated life-time for the powder sample was equal $\tau = 0.07$ ns, indicating a strong fluorescence aggregation-induced quenching.[43] It is caused by π–π intermolecular stacking of the $p(C_3O_2)_x$ in bulk phase, limiting its application as OLEDs.[44] Nonetheless, this behavior is promising for photocatalytic applications, where short emission lifetimes are often associated with the presence of non-radiative long-lived excited state species.[45] The best examples are carbon nitrides, which also show highly quenched PL and similar average amplitude lifetimes.[46]

Both UV–vis absorption and PL data point to a complex electronic structure of the aggregated form of the $p(C_3O_2)_x$ where phenomena like excitonic coupling might take place. Moreover, a significant PL shift indicates strong intermolecular π–π interactions in the aggregated form.[47]

2.5. Photocatalytic Activity

The medium bandgap and polypyrone structure mimicking that of coumarin dyes[48] are two indicators which point to red carbon as a promising photocatalyst. Therefore, the photocatalytic performance of red carbon was tested in model reactions and compared to other state-of-the-art photocatalysts, such as carbon nitrides (graphitic g-CN and mesoporous graphitic mpg-CN), potassium and sodium poly(heptazine imides) (K-PHI and Na-PHI, respectively), and commercial organometallic homogenous catalysts tris(2-phenylpyridine)iridium(III) ($Ir(ppy)_3$) and tris(bipyridine)ruthenium(II) chloride ($[Ru(bpy)_3]Cl_2$) (**Figure 6**). We tested the oxidation of thioanisole (1a) and benzylalcohol (2b) by irradiating with blue light reaction mixtures containing substrates, catalysts, and oxygen. The summary showing the conversion and the amount of generated products for each catalyst are presented in Figure 6 and Tables S2 and S3, Supporting Information. In the oxidation of thioanisole (1b), red carbon produced sulfoxide 1b in 40% yield and sulfone 1c in 57% yield, while the oxidation of benzyl alcohol resulted in 74% yield of benzaldehyde (2b). The oxidation of 1a is less selective compared to benzyl alcohol due to faster conversion of the substrate, leading to consecutive oxidation of sulfoxide 1b to sulfone 1c.[49]

Nevertheless, red carbon showed the best selectivities and conversions among the tested photocatalysts. In the case of benzyl alcohol oxidation to benzaldehyde, red carbon showed over 50% better conversion than almost all other photocatalysts

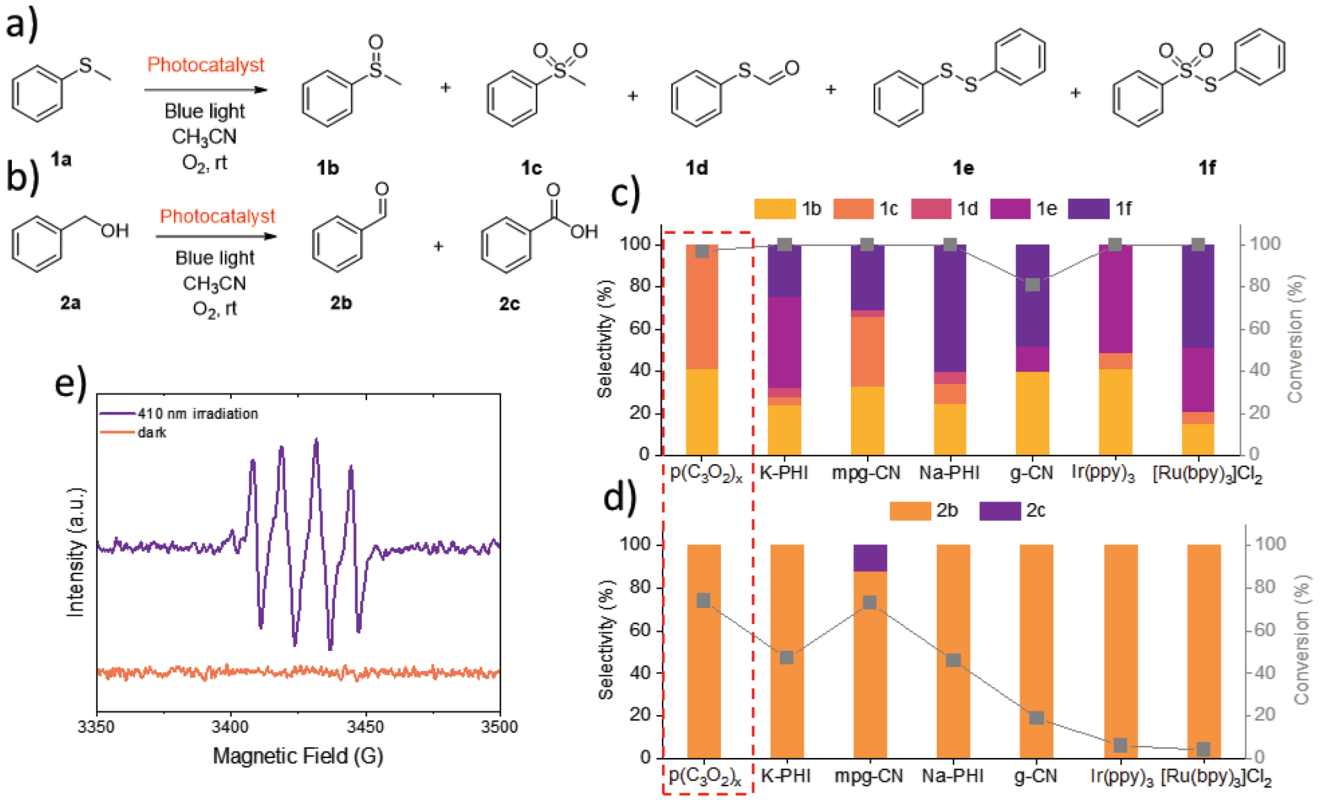

Figure 6. a,b) Photocatalytic benchmark reactions. Reaction conditions: thioanisole 1a (2.5 µL, 0.020 mmol) or benzylic alcohol 2a (2.5 µL, 0.025 mmol), CH_3CN (3 mL), O_2 (1 bar), blue LED (468 nm, 14 mW cm^{-2}), 24 h reaction time. See the experimental procedure for details in the Supporting Information. Yields determined via GC-MS (Figure S20, Supporting Information). c,d) Comparison of the performance of different photocatalysts (including red carbon) in oxidation of anisole (c) and benzyl alcohol (d). e) EPR studies of a reaction mixture with DMPO as a spin-trap agent.

with ≈100% selectivity. For oxidation of thioanisole, the conversion has been the same as for the rest of the catalysts. However, $p(C_3O_2)_x$ exhibited enhanced selectivity. The benchmark photocatalysts formed a mixture of three or more compounds, while red carbon favored the formation of only sulfone and sulfoxide in a 3:2 molar ratio.

Such oxidations are exclusively triggered by reactive oxygen species such as $^1O_2$ or $O_2^{\bullet-}$ which are generated in situ via photocatalytic pathway,[50] and as proved by the control experiments (Tables S4 and S5, Supporting Information). It means that poly(carbon suboxide) acts as a sensitizer by generating $^1O_2$,[50] or via photoredox chemistry, generating $O_2^{\bullet-}$.[51] To distinguish the principal mechanism of oxidation, we performed EPR studies under light irradiation in the presence of spin trapping agent DMPO (5,5-dimethyl-1-pyrro-line-N-oxide) and the results are summarized in Figure 6e. Under illumination, a relatively strong EPR signal appears already after 1 min. The signal is typical for anion adducts of the superoxide anion with DMPO ($DMPO\text{-}^{\bullet}O_2^-/^{\bullet}O_2H$) with quadruplet peaks with an intensity ratio close to 1:1:1:1. The hyperfine fit parameters calculated for the adduct were $a_N = 13.0$ G and $a_{H\beta} = 10.4$ G which match the $DMPO\text{-}^{\bullet}O_2^-/^{\bullet}O_2H$ adducts reported in the literature in acetonitrile solvent.[52,53] Without the irradiation, no signal appears. This means that oxidation of thioanisole and benzyl alcohol occurred by means of superoxide radical. Considering the superior performance of red carbon as a photocatalyst in comparison to benchmark ones, the material has the potential to enable a range of other transformations.

3. Conclusions

The condensation of C_3O_2 is a simple approach for synthesizing conjugated ladder polymers in a single step. The peculiar bonding motif of the monomer allows obtaining highly conjugated structures at comparably low condensation temperatures. In this work, we managed to transfer this elegant chemistry into the liquid phase in which the C_3O_2 forms and condenses into $p(C_3O_2)_x$. Both structural and chemical analyses prove the formation of an oligomeric semiconductor made of polypyrone ribbons. In contrast to previous synthetic methods, this "in-solution" approach results in well-defined and crystalline structures. Importantly, the $p(C_3O_2)_x$ covalent structure is equivalent to polyacetylene (one of the most conductive polymers) limited by —O—C(O)— groups. In contrast to many other organic semiconductors, $p(C_3O_2)_x$ is soluble and can be easily deposited in the form of films, therefore, holding great potential to solve the processing problems of polyacetylenes. Further theoretical and optical studies confirmed that the material has a medium-sized direct band gap. Since these properties are very appealing for photocatalysis, we performed two photocatalytic oxidations as a proof of concept. Indeed, benzyl alcohol and thioanisol were

successfully converted to benzaldehyde and phenylsulfoxyde/sulfone in good yields. The chemistry of C_3O_2 also presents interesting pathways for future development of carbonaceous materials via soft-chemical approaches. It does not possess any C—H bonds and thus holds tremendous potential as a starting material for smart condensation–aromatization routes.

4. Experimental Section

Synthesis: In a typical synthesis, a specific molar ratio of malonic acid and AAn were mixed in a glass round-bottom flask. For instance, for sample 1:2_140 °C, 10 g of malonic acid was mixed with 19.6 g of AAn in a 100 ml flask. The mixture was first heated to 90 °C in a heating mantle for 15 min to dissolve the malonic acid. Subsequently, the temperature was raised to either 110 or 140 °C and kept for 5 h. During this time, the solution was stirred by a magnetic stirrer and kept under reflux. The resulting viscous solution was slowly dropped into a 500 mL flask containing 200 mL of diethyl ether to complete the precipitation and subsequently, the product was vacuum-filtrated. Then, the powder was dried and redispersed in diethyl ether and filtrated again. The procedure was repeated three times. Alternatively, the powder could be washed by applying Soxhlet extraction with diethyl ether. Then the powder was vacuum dried at 90 °C overnight. Such a purified sample was used for further analyses.

Characterizations: FTIR spectroscopy was carried out using a Thermo Scientific Nicolet iD5 spectrometer with the attenuated total reflection sampling technique. Raman spectroscopy was performed on a Witec Alpha 300M+ instrument with a 488 nm laser and microscope objective 100×; the spectra were accumulated 100 times for 5 s. The morphology and composition of the sample were studied by SEM using a Zeiss Gemini 1550 microscope equipped with an Oxford Instruments EDX analyzer. The samples were covered with a thin layer of Au to enhance the surface conductivity and reduce the charging effect during analysis.

For transmission electron microscopy (TEM), a suspension of the sample in ethanol was sonicated for 10 min and then drop-casted to a Cu grid with a holey carbon support and dried for 30 min. The TEM study was performed using a double Cs corrected JEOL JEM-ARM200F (S)TEM operated at 80 kV and equipped with a cold-field emission gun.

The sample crystallinity was determined by powder XRD performed on Bruker D8 Advance Instrument with Cu Kα irradiation. XPS measurements were performed on a Thermo Scientific Escalab 250 Xi instrument. A micro-focused, monochromated Al Kα X-ray source (1486.68 eV) and a 400 µm spot size were used. The powder samples were dispersed in THF and drop-casted onto clean silicon wafers and vacuum dried at room temperature. The binding energies were calibrated toward Si. The Thermo Scientific Avantage software was used to analyze the resulting spectra. TGA was performed in the range of 25–1000 °C using a NETZSCHTG 209 F1 device. Samples were heated in an Al_2O_3 crucible using nitrogen atmosphere and a heating rate of 10 °C min^{-1}. The sample porosity was measured by N_2 sorption at 77 K using a Quantachrome Quadrasorb SI apparatus. ^{1}H NMR spectra were recorded on an Agilent 400 MHz spectrometer by dissolving the sample in deuterated THF. Optical absorbance spectra were recorded on a Shimadzu UV 2600 spectrometer using an integrating sphere for diffusive reflectance spectroscopy. Photoluminescence spectra were measured on an FP-8300 fluorescence spectrometer. Emission lifetimes decays were measured using C-SPC, using PicoQuant FluoTime 250 with 375 nm laser diode excitation. Each sample was measured using the wavelength of the strongest light emission determined by PL experiments: a) in a diluted NMP solution (0.01 mg mL^{-1}) (λ_{EM} = 480 nm); b) in solid state (λ_{EM} = 680 nm); of films (λ_{EM} = 670 nm).

^{13}C magic angle spinning nuclear magnetic resonance (MAS-NMR) measurements were carried out at 25 °C, using a Tecmag Apollo spectrometer equipped with a wide-bore 300 MHz Oxford magnet. The resonance frequency of ^{13}C was 75.394 MHz. A Bruker MAS probe for 4 mm ZrO rotors was used; the spinning frequency was set to 10 kHz. Proton decoupled ^{13}C NMR measurements were recorded using a recycling delay of 50 s, an excitation pulse length of 3.5 µs, and a dwell time of 10 µs. The time domain signals were averaged over 1000 scans. To suppress possible background signals, background subtraction was employed by first measuring the spectrum of the sample and then recording the signal of an empty rotor using the same experimental parameters. ^{13}C spectra were externally referenced to the methylene carbon signal of adamantane at 29.5 ppm. The chemical shifts reported had an error of ±0.1 ppm. EPR studies were carried out on Bruker EMXnano benchtop X-Band EPR spectrometer. For the seetings, Modulation Amplitude 1.000 G, Microwave attenuation 10 dB, and Receiver Gain 60 dB were used.

Photocatalytic Studies: Mass spectral data were obtained using an Agilent GC 6890 gas chromatograph, equipped with an HP-5MS column (inner diameter = 0.25 mm, length = 30 m, and film = 0.25 µm), coupled with Agilent MSD 5975 mass spectrometer (electron ionization). The irradiance of LED modules was measured using a PM400 Optical Power and Energy Meter equipped with the integrating sphere S142C and purchased from Thorlabs. A blue LED module was used to perform photocatalytic experiments (home-made steel cylinder photoreactor attached with self-adhesive LED strips which were purchased from JKL components, emission maximum λ = 468 nm, measured optical power 14 mW cm^{-2} at the central position).

Standard Procedure for Photocatalytic Experiments: In a 4 mL vial, thioanisole 1a (2.5 µL, 0.020 mmol) or benzylic alcohol 2a (2.5 µL, 0.025 mmol) in CH_3CN (3 mL) were added and closed with a rubber screw cap. The solution was flushed via double needle technique with O_2 for 2 min. The vial was placed under irradiation of blue LED modules for 24 h. Yield and conversion were quantified by GC-MS.

Benchmark Photocatalysts: Carbon nitride and poly(heptazine imide) photocatalysts were synthesized according to previous reports (K-PHI,[54] Na-PHI,[55] mpg-CN,[56] g-CN[2]). $Ir(ppy)_3$ and $[Ru(bpy)_3]Cl_2$ were purchased from Sigma Aldrich.

Computational Details: Periodic DFT calculations were carried out using the hybrid Gaussian and plane wave approach,[57] as implemented in the CP2K/Quickstep code.[34] The Kohn–Sham orbitals were described by an accurate molecularly optimized double-zeta basis set with one additional set of polarization functions,[58] while the charge density was represented by plane waves with a density cutoff of 500 Ry. The B97-D exchange and correlation functional, based on Becker's power-series Ansatz, plus a damped atom-pairwise dispersion correction to account for long-range van der Waals interactions was employed.[59] Separable norm-conserving pseudopotentials were used to mimic the interactions between the valence electrons and the ionic cores.[60] The structure of $p(C_3O_2)_x$ was modeled using a supercell with a = 25.0, b = 37.0, and c = 7.4 Å and $\alpha = \beta = \gamma$ = 90.0°, which contained 2 × 4 C_3O_2 polypyron chains consisting of six monomeric units each. Optimized structures were obtained by globally minimizing the potential energy, while varying the atomic positions by dynamical simulated annealing based on the second-generation Car–Parrinello approach of Kühne et al.[33,61,62] To compute the net atomic charges and bond orders of the obtained structures, the density-derived electrostatic and chemical method DDEC6 was used.[35]

Supporting Information

Supporting Information is available from the Wiley Online Library or from the author.

Acknowledgements

M.O. acknowledges the Alexander von Humboldt Stifung for financial support. Max Planck Society is gratefully acknowledged for its financial support. This work was supported by MoMa-STOR ERC-2020-SyG ID: 951513. The authors acknowledge Prof. Maciej Sitarz and Dr. Piotr Jelen

(University of Science and Technology AGH in Cracow, Poland) for performing Raman spectroscopy and fruitful discussion. Also, L.P.-T. and D.N. acknowledge funding by the DFG (HIOS (Project number 182087777 – SFB 951).

Open access funding enabled and organized by Projekt DEAL.

Conflict of Interest

The authors declare no conflict of interest.

Data Availability Statement

The data that support the findings of this study are available from the corresponding author upon reasonable request.

Keywords

carbon suboxide, carbonaceous materials, conjugated ladder polymers, covalent materials, photocatalysts

Received: July 14, 2022
Published online: September 3, 2022

[1] T. Banerjee, F. Podjaski, J. Kröger, B. P. Biswal, B. V. Lotsch, *Nat. Rev. Mater.* **2021**, *6*, 168.
[2] X. Wang, K. Maeda, A. Thomas, K. Takanabe, G. Xin, J. M. Carlsson, K. Domen, M. Antonietti, *Nat. Mater.* **2009**, *8*, 76.
[3] S. Bi, C. Yang, W. Zhang, J. Xu, L. Liu, D. Wu, X. Wang, Y. Han, Q. Liang, F. Zhang, *Nat. Commun.* **2019**, *10*, 2467.
[4] J. Lee, A. J. Kalin, T. Yuan, M. Al-Hashimi, L. Fang, *Chem. Sci.* **2017**, *8*, 2503.
[5] A. Narita, X. Y. Wang, X. Feng, K. Müllen, *Chem. Soc. Rev.* **2015**, *44*, 6616.
[6] X. Yang, X. Dou, A. Rouhanipour, L. Zhi, H. J. Räder, K. Müllen, *J. Am. Chem. Soc.* **2008**, *130*, 4216.
[7] J. Cai, P. Ruffieux, R. Jaafar, M. Bieri, T. Braun, S . Blankenburg, M. Muoth, A. P. Seitsonen, M. Saleh, X. Feng, K. Müllen, R. Fasel, *Nature* **2010**, *466*, 470.
[8] N. Lopez-Salas, J. Kossmann, M. Antonietti, *Acc. Mater. Res.* **2020**, *1*, 117.
[9] B. C. Brodie, *Philos. Trans. R. Soc. London* **1874**, *164*, 83.
[10] H. Staudinger, S. Bereza, *Ber. Dtsch. Chem. Ges.* **1908**, *41*, 4461.
[11] O. Diels, B. Wolf, *Ber. Dtsch. Chem. Ges.* **1906**, *39*, 689.
[12] A. R. Blake, W. T. Eeles, P. P. Jennings, *Eur. Polym. J.* **1963**, *60*, 691.
[13] A. W. Snow, H. Haubenstock, N. L. Yang, *Macromolecules* **1978**, *11*, 77.
[14] T. Carofiglio, L. Pandolfo, G. Paiaro, *Eur. Polym. J.* **1986**, *22*, 491.
[15] R. N. Smith, D. A. Young, E. N. Smith, C. C. Carter, *Inorg. Chem.* **1963**, *2*, 829.
[16] J. S. auf der Günne, J. Beck, W. Hoffbauer, P. Krieger-Beck, *Chem. – Eur. J.* **2005**, *11*, 4429.
[17] V. C. Fäseke, F. C. Raps, C. Sparr, *Angew. Chem., Int. Ed.* **2020**, *59*, 6975.
[18] Q. Cao, B. Kumru, M. Antonietti, B. V. K. J. Schmidt, *Mater. Horiz.* **2020**, *7*, 762.
[19] Y. Xu, Y. Cui, H. Yao, T. Zhang, J. Zhang, L. Ma, J. Wang, Z. Wei, J. Hou, *Adv. Mater.* **2021**, *33*, 2101090.
[20] M. Carroli, A. G. Dixon, M. Herder, E. Pavlica, S. Hecht, G. Bratina, E. Orgiu, P. Samorì, *Adv. Mater.* **2021**, *33*, 2007965.
[21] L. Liu, Y. Kan, K. Gao, J. Wang, M. Zhao, H. Chen, C. Zhao, T. Jiu, A. K. Y. Jen, Y. Li, *Adv. Mater.* **2020**, *32*, 1907604.
[22] S. Mazzanti, A. Savateev, *ChemPlusChem* **2020**, *85*, 2499.
[23] H. M. Perks, J. F. Liebman, *Struct. Chem.* **2000**, *11*, 265.
[24] M. Ballauff, S. Rosenfeldt, N. Dingenouts, J. Beck, P. Krieger-Beck, L. Li, *Angew. Chem., Int. Ed.* **2004**, *43*, 5843.
[25] S. Kundu, A. K. Naskar, A. A. Ogale, D. P. Anderson, J. R. Arnold, *Carbon* **2008**, *46*, 1166.
[26] C. Tschierske, *J. Mater. Chem.* **1998**, *8*, 1485.
[27] P. J. Repasky, D. M. Agra-Kooijman, S. Kumar, C. S. Hartley, *J. Phys. Chem. B* **2016**, *120*, 2829.
[28] B. Wunderlich, S. N. Kreitmeier, *MRS Bull.* **1995**, *20*, 17.
[29] M. Acik, G. Lee, C. Mattevi, M. Chhowalla, K. Cho, Y. J. Chabal, *Nat. Mater.* **2010**, *9*, 840.
[30] D. B. Schuepfer, F. Badaczewski, J. M. Guerra-Castro, D. M. Hofmann, C. Heiliger, B. Smarsly, P. J. Klar, *Carbon* **2020**, *161*, 359.
[31] H. E. Schaffer, R. R. Chance, R. J. Silbey, K. Knoll, R. R. Schrock, *J. Chem. Phys.* **1991**, *94*, 4161.
[32] H. Shirakawa, T. Ito, S. Ikeda, *Polym. J.* **1973**, *4*, 460.
[33] T. D. Kühne, M. Krack, F. R. Mohamed, M. Parrinello, *Phys. Rev. Lett.* **2007**, *98*, 066401.
[34] T. D. Kühne, M. Iannuzzi, M. Del Ben, V. V. Rybkin, P. Seewald, F. Stein, T. Laino, R. Z. Khaliullin, O. Schütt, F. Schiffmann, D. Golze, J. Wilhelm, S. Chulkov, M. H. Bani-Hashemian, V. Weber, U. Borštnik, M. Taillefumier, A. S. Jakobovits, A. Lazzaro, H. Pabst, T. Müller, R. Schade, M. Guidon, S. Andermatt, N. Holmberg, G. K. Schenter, A. Hehn, A. Bussy, F. Belleflamme, G. Tabacchi, et al., *J. Chem. Phys.* **2020**, *152*, 194103.
[35] T. A. Manz, N. G. Limas, *RSC Adv.* **2016**, *6*, 47771.
[36] H. Huang, L. Yang, A. Facchetti, T. J. Marks, *Chem. Rev.* **2017**, *117*, 10291.
[37] A. A. B. Alghamdi, D. C. Watters, H. Yi, S. Al-Faifi, M. S. Almeataq, D. Coles, J. Kingsley, D. G. Lidzey, A. Iraqi, *J. Mater. Chem. A* **2013**, *1*, 5165.
[38] M. S. Vezie, S. Few, I. Meager, G. Pieridou, B. Dörling, R. S. Ashraf, A. R. Goñi, H. Bronstein, I. McCulloch, S. C. Hayes, M. Campoy-Quiles, J. Nelson, *Nat. Mater.* **2016**, *15*, 746.
[39] J. K. Gallaher, K. Chen, G. S. Huff, S. K. K. Prasad, K. C. Gordon, J. M. Hodgkiss, *J. Phys. Chem. Lett.* **2016**, *7*, 3307.
[40] Z. Hu, A. P. Willard, R. J. Ono, C. W. Bielawski, P. J. Rossky, D. A. Vanden Bout, *Nat. Commun.* **2015**, *6*, 8246.
[41] H. Bässler, B. Schweitzer, *Acc. Chem. Res.* **1999**, *32*, 173.
[42] K. O. Brinkmann, T. Becker, F. Zimmermann, C. Kreusel, T. Gahlmann, M. Theisen, T. Haeger, S. Olthof, C. Tückmantel, M. Günster, T. Maschwitz, F. Göbelsmann, C. Koch, D. Hertel, P. Caprioglio, F. Peña-Camargo, L. Perdigón-Toro, A. Al-Ashouri, L. Merten, A. Hinderhofer, L. Gomell, S. Zhang, F. Schreiber, S. Albrecht, K. Meerholz, D. Neher, M. Stolterfoht, T. Riedl, *Nature* **2022**, *604*, 280.
[43] Y. Huang, J. Xing, Q. Gong, L. C. Chen, G. Liu, C. Yao, Z. Wang, H. L. Zhang, Z. Chen, Q. Zhang, *Nat. Commun.* **2019**, *10*, 169.
[44] Y. Chen, J. W. Y. Lam, R. T. K. Kwok, B. Liu, B. Z. Tang, *Mater. Horiz.* **2019**, *6*, 428.
[45] A. Savateev, I. Ghosh, B. König, M. Antonietti, *Angew. Chem., Int. Ed.* **2018**, *57*, 15936.
[46] Y. Markushyna, C. M. Schüßlbauer, T. Ullrich, D. M. Guldi, M. Antonietti, A. Savateev, *Angew. Chem., Int. Ed.* **2021**, *60*, 20543.
[47] Y. Dong, B. Xu, J. Zhang, X. Tan, L. Wang, J. Chen, H. Lv, S. Wen, B. Li, L. Ye, B. Zou, W. Tian, *Angew. Chem., Int. Ed.* **2012**, *51*, 10782.
[48] A. Gualandi, G. Rodeghiero, E. Della Rocca, F. Bertoni, M. Marchini, R. Perciaccante, T. P. Jansen, P. Ceroni, P. G. Cozzi, *Chem. Commun.* **2018**, *54*, 10044.

[49] V. R. Tumula, S. Bondwal, P. Bisht, C. Pendem, J. Kumar, *React. Kinet., Mech. Catal.* **2012**, *107*, 449.
[50] S. Mazzanti, G. Manfredi, A. J. Barker, M. Antonietti, A. Savateev, P. Giusto, *ACS Catal.* **2021**, *11*, 11109.
[51] Y. Markushyna, C. Teutloff, B. Kurpil, D. Cruz, I. Lauermann, Y. Zhao, M. Antonietti, A. Savateev, *Appl. Catal., B* **2019**, *248*, 211.
[52] J. R. Harbour, M. L. Hair, *J. Phys. Chem.* **1978**, *82*, 1397.
[53] R. Dabestani, R. D. Hall, R. H. Sik, C. F. Chignell, *Photochem. Photobiol.* **1990**, *52*, 961.
[54] A. Savateev, D. Dontsova, B. Kurpil, M. Antonietti, *J. Catal.* **2017**, *350*, 203.
[55] Z. Chen, A. Savateev, S. Pronkin, V. Papaefthimiou, C. Wolff, M. G. Willinger, E. Willinger, D. Neher, M. Antonietti, D. Dontsova, *Adv. Mater.* **2017**, *29*, 1700555.
[56] I. Ghosh, J. Khamrai, A. Savateev, N. Shlapakov, M. Antonietti, B. König, *Science* **2019**, *365*, 360.
[57] G. Lippert, J. Hutter, M. Parrinello, *Mol. Phys.* **1997**, *92*, 477.
[58] J. VandeVondele, J. Hutter, *J. Chem. Phys.* **2007**, *127*, 114105.
[59] E. Perlt, P. Ray, A. Hansen, F. Malberg, S. Grimme, B. Kirchner, *J. Chem. Phys.* **2018**, *148*, 193835.
[60] S. Goedecker, M. Teter, *Phys. Rev. B* **1996**, *54*, 1703.
[61] T. D. Kühne, *WIREs Comput. Mol. Sci.* **2014**, *4*, 391.
[62] T. D. Kühne, E. Prodan, *Ann. Phys.* **2018**, *391*, 120.